ORIGINAL PAPER

An analytical solution of scattering of semi-circular hill on cylindrical SH waves

Zhiwen Li[1,2] · Haibo Li[1,2]

Abstract

Irregular topography can induce scattering and diffraction of incident seismic waves and cause topographic amplification effects. In this paper, a theoretical model for the scattering and diffraction of cylindrical SH waves caused by a semi-circular hill is established for the first time to reveal the influence of source characteristics on the topographic amplification effects. The analytical solution of the theoretical model is derived via the wave function expansion method and image theory, and its accuracy is verified by checking the given boundary conditions. Base on the presented solution, the influences of source location, incident wave frequency, and hill radius on amplitude amplification are systematically investigated. Comparison of amplitude amplification around the hill caused by cylindrical waves and plane waves indicates that the effect of source distance on topographic amplification effects is not negligible unless the source distance exceeds 15 times the hill radius. It suggests that much attention should be paid to the effects of source location on topographic amplification effects, especially when the source is near the topography.

Keywords Scattering and diffraction · Topographic amplification effects · Cylindrical SH waves · Semi-circular hill · Wave function expansion method

Introduction

Irregular topography can induce the scattering and diffraction of incident seismic waves, which markedly alters the travel law of seismic waves. Field observations and model experiments have shown that in some cases, the vibration amplitudes of irregular topography are much greater than those of flat topography, exhibiting significant topographic amplification effects (Trifunac and Hudson 1971; Hough et al. 2010; Massa et al. 2014; Li et al. 2019b). Strong vibration can cause damage to buildings and even endanger human life, therefore studying wave scattering and diffraction induced by irregular topography has been one of the most important subjects in earthquake engineering (Geli et al. 1988; Ferraro et al. 2009).

Considering that field observations and model experiments can only give some qualitative analysis, extensive numerical and analytical methods have been employed to deepen the understanding of wave scattering induced by irregular topography. The numerical methods mainly include finite element method (Komatitsch and Vilotte 1998; Cavallaro et al. 2008; Li et al. 2019a), finite difference method (Boore 1972; Opršal and Zahradník 1999), and boundary element method (Wong and Jennings 1975; Panji et al. 2014). The numerical methods are convenient to address the wave scattering problems with complex surface geometries and geological conditions, but its accuracy depends on the quality of meshes which will inevitably introduce numerical errors. In contrast, the analytical methods are only capable of tackling a few simple wave scattering problems, while they can provide us a profound understanding of the mechanism of wave scattering and test the accuracy of numerical methods, hence obtaining an analytical solution is very encouraging. The analytical methods mainly include wave function expansion method, integral equation method, and perturbation method (Mow and Pao 1971). The wave function expansion method is the most widely employed due to its high precision and relatively simple mathematical derivation.

✉ Haibo Li
  hbli@whrsm.ac.cn

1   State Key Laboratory of Geomechanics and Geotechnical Engineering, Institute of Rock and Soil Mechanics, Chinese Academy of Sciences, Wuhan 430071, China

2   University of Chinese Academy of Sciences, Beijing 100049, China

At present, most theoretical studies on this subject presuppose the incident seismic waves as plane waves, and there are several analytical solutions to the scattering of plane *SH* waves caused by various-shaped concave topographies (Trifunac 1972; Wong and Trifunac 1974; Cao and Lee 1989; Yuan and Liao 1994; Tsaur and Chang 2008, 2010; Zhang et al. 2012a, 2012b; Gao et al. 2012; Le et al. 2017) and convex topographies (Yuan and Men 1992; Yuan and Liao 1996; Lee et al. 2006; Hayir et al. 2001; Qiu and Liu 2005; Lin et al. 2010; Amornwongpaibun and Lee 2013; Lee and Amornwongpaibun 2013). Besides, a few analytical solutions to the scattering of plane *P, SV* and Rayleigh waves caused by irregular topography, have been presented (Lee and Cao 1989; Cao and Lee 1990; Todorovska and Lee 1991; Liang et al. 2005a, 2005b, 2006).

It is acceptable to treat the incident seismic waves as plane waves when the earthquake source is far away from the irregular topography. However, when the earthquake source is located in the vicinity of irregular topography, the wavefront curvature of incident seismic waves is considerable, resulting in the propagation path of incident seismic waves and plane waves significantly different. In such case, the effects of source location on wave scattering induced by irregular topography should be taken into account. To theoretically study the effects of source location on wave scattering, the incident seismic waves can be assumed as spherical waves or cylindrical waves, and several analytical solutions have been proposed for the scattering of cylindrical *SH* waves caused by concave topographies (Gao and Zhang 2013; Zhang et al. 2015). However, as far as we know, analytical solutions for cylindrical *SH* wave scattering caused by convex topographies are rare. Herein, we present an analytical solution on the scattering of cylindrical *SH* waves caused by a semi-circular hill, aiming to reveal the effects of earthquake source on wave scattering by convex topographies. The specific process of this paper is given as follows. Firstly, the model of a semi-circular hill on an elastic half-space subject to a buried anti-plane line source is established, and the corresponding series solution is derived through the wave function expansion method and image theory. Secondly, the relationship between the accuracy of the series solution and its truncation orders is discussed by checking the residuals of boundary conditions. Lastly, based on the series solution, the effects of source location, incident wave frequency, and hill radius on vibration amplitudes of the surface and interior of the hill are systematically discussed.

Theoretical formula

The 2D theoretical model in this study is depicted in Fig. 1. This figure illustrates a semi-circular hill with radius *a* sitting on an elastic, isotropic, and homogeneous half-space, with
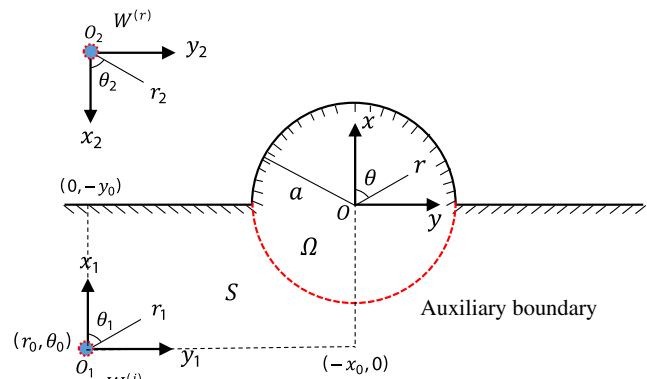
Fig. 1 Schematic diagram of the theoretical model of a semi-circular hill subjected to a buried anti-plane line source

buried anti-plane line source below the hill. The material properties of the model are given by the shear modulus μ and shear wave velocity c.

To simplify the issue, we divide the theoretical model into an exterior region S and an interior region Ω by a semi-circular auxiliary boundary as shown in Fig. 1 (Yuan and Men 1992). In these two regions, two Cartesian and two polar coordinate systems are defined. Both origins of the Cartesian coordinate system (x, y) and polar coordinate system (r, θ) are set at the center of hill bottom. The origins of the Cartesian coordinate system (x_1, y_1) and polar coordinate system (r_1, θ_1) are placed at the line source. The horizontal y-axis (or y_1-axis) is set as positive to the right direction, and the angles θ (or θ_1) are measured from the vertical direction x-axis (or x_1-axis) clockwise towards to the y-axis (or y_1-axis). The location of the line source is denoted by (r_0, θ_0) in the polar coordinate system (r, θ) and $(-x_0, -y_0)$ in the Cartesian coordinate system (x, y). For the issue studied herein, we set a virtual line source for the reflected wave generated by the half-space. The origins of the Cartesian coordinate system (x_2, y_2) and polar coordinate system (r_2, θ_2) are placed at the virtual line source, and the angle θ_2 is measured from the vertical direction x_2-axis anticlockwise towards to the horizontal direction y_2-axis.

The displacement field W within the entire model must satisfy the elastic-wave equation:

$$\frac{\partial^2 W}{\partial r^2} + \frac{1}{r}\frac{\partial W}{\partial r} + \frac{1}{r^2}\frac{\partial^2 W}{\partial \theta^2} + k^2 W = \frac{\delta(r-r_0)\delta(\theta-\theta_0)}{r} \qquad (1)$$

where $\delta(\cdot)$ is the Dirac delta function, $k = \omega/c$ is the wavenumber, and ω is the circular frequency. The time factor $\exp(-i\omega t)$ has been omitted for the steady waves.

Besides, the displacement fields should satisfy the traction-free boundary condition on the horizontal ground surface and hill surface:

$$\tau_{\theta z} = \frac{\mu \partial W}{r \partial \theta} = 0, \qquad \theta = \pm \pi/2, \qquad r > a \qquad (2)$$

$$\tau_{rz} = \frac{\mu \partial W}{\partial r} = 0, \quad -\pi/2 < \theta < \pi/2, \quad r = a \quad (3)$$

Considering that the exterior region S and interior region Ω are welded together, the continuities of displacement and stress at the auxiliary boundary are also required:

$$\begin{cases} W^{(\Omega)}(a, \theta) = W^{(S)}(a, \theta) \\ \tau_{rz}^{(\Omega)}(a, \theta) = \tau_{rz}^{(S)}(a, \theta) \end{cases}, -\pi \leq \theta \leq -\frac{\pi}{2} \cup \frac{\pi}{2} \leq \theta \leq \pi \quad (4)$$

The incident wave $W^{(i)}$ is emitted by the line source, and its mathematical form in polar coordinate system (r_1, θ_1) is as follows:

$$W^{(i)} = \frac{i}{4\mu} H_0^{(1)}(kr_1) \quad (5)$$

where $H_0^{(1)}(\cdot)$ represents the Hankel function of the first kind with order 0.

Based on the image theory, the reflected wave $W^{(r)}$ induced by the half-space can be written in polar coordinate system (r_2, θ_2) as follows:

$$W^{(r)} = \frac{i}{4\mu} H_0^{(1)}(kr_2) \quad (6)$$

According to coordinate relations:

$$x_2 = 2x_0 - x_1, y_2 = y_1 \quad (7)$$

$$x_1 = x + x_0, y_1 = y + y_0 \quad (8)$$

The incident wave $W^{(i)}$ and the reflected wave $W^{(r)}$ can be rewritten in the Cartesian coordinate system (x, y) as follows:

$$W^{(i)} = \frac{i}{4\mu} H_0^{(1)}\left(k\sqrt{x^2 + y^2 + 2x_0 x + 2y_0 y + x_0^2 + y_0^2}\right) \quad (9)$$

$$W^{(r)} = \frac{i}{4\mu} H_0^{(1)}\left(k\sqrt{x^2 + y^2 - 2x_0 x + 2y_0 y + x_0^2 + y_0^2}\right) \quad (10)$$

We can define $W^{(ff)} = W^{(i)} + W^{(r)}$ as a free-field displacement which represents the displacement of half-space at the absence of the hill, and its mathematical form in polar coordinate system (r, θ) is as follows:

$$W^{(ff)} = \frac{i}{4\mu}\left[H_0^{(1)}\left(k\sqrt{r^2 + 2x_0 r\cos\theta + 2y_0 r\sin\theta + x_0^2 + y_0^2}\right) + H_0^{(1)}\left(k\sqrt{r^2 - 2x_0 r\cos\theta + 2y_0 r\sin\theta + x_0^2 + y_0^2}\right)\right] \quad (11)$$

And, relevant stress components are derived as follows:

$$\tau_{\theta z}^{(ff)} = \frac{\mu \partial W^{(ff)}}{r \partial \theta} = \frac{ik}{4r}\left\{H_0'^{(1)}\left(k\sqrt{r^2 + 2x_0 r\cos\theta + 2y_0 r\sin\theta + x_0^2 + y_0^2}\right)\frac{-x_0 r\sin\theta + y_0 r\cos\theta}{\sqrt{r^2 + 2x_0 r\cos\theta + 2y_0 r\sin\theta + x_0^2 + y_0^2}} \right.$$
$$\left. + H_0'^{(1)}\left(k\sqrt{r^2 - 2x_0 r\cos\theta + 2y_0 r\sin\theta + x_0^2 + y_0^2}\right)\frac{x_0 r\sin\theta + y_0 r\cos\theta}{\sqrt{r^2 - 2x_0 r\cos\theta + 2y_0 r\sin\theta + x_0^2 + y_0^2}}\right\} \quad (12)$$

$$\tau_{rz}^{(ff)} = \frac{\mu \partial W^{(ff)}}{\partial r} = \frac{ik}{4}\left\{H_0'^{(1)}\left(k\sqrt{r^2 + 2x_0 r\cos\theta + 2y_0 r\sin\theta + x_0^2 + y_0^2}\right)\frac{r + x_0\cos\theta + y_0\sin\theta}{\sqrt{r^2 + 2x_0 r\cos\theta + 2y_0 r\sin\theta + x_0^2 + y_0^2}} \right.$$
$$\left. + H_0'^{(1)}\left(k\sqrt{r^2 - 2x_0 r\cos\theta + 2y_0 r\sin\theta + x_0^2 + y_0^2}\right)\frac{r - x_0\cos\theta + y_0\sin\theta}{\sqrt{r^2 - 2x_0 r\cos\theta + 2y_0 r\sin\theta + x_0^2 + y_0^2}}\right\} \quad (13)$$

where $H_0'^{(1)}(\cdot)$ is the first derivative of $H_0^{(1)}(\cdot)$.

Substituting $\theta = \pm\,\pi/2$ into Eq. (12) deduces $\tau_{\theta z}^{(ff)} = 0$ which means the free-field displacement $W^{(ff)}$ satisfy the traction-free boundary condition Eq. (2).

Since the expressions of $W^{(ff)}$ and $\tau_{rz}^{(ff)}$ are quite complex, further derivation via the separation variable method in this study is cumbersome. We expand $W^{(ff)}$ and $\tau_{rz}^{(ff)}$ into Fourier series over the interval $[-\pi,\pi]$ as follows:

$$W^{(ff)} = \sum_{m=0}^{+\infty} M_m\cos m\theta + N_m\sin m\theta \qquad (14)$$

$$\tau_{rz}^{(ff)} = \mu k \sum_{m=0}^{+\infty} M'_m\cos m\theta + N'_m\sin m\theta \qquad (15)$$

where

$$\begin{cases} M_m = \dfrac{1}{\Delta_m\pi}\int_{-\pi}^{\pi}W^{(ff)}\cos m\theta d\theta, \\[2mm] N_m = \dfrac{1}{\pi}\int_{-\pi}^{\pi}W^{(ff)}\sin m\theta d\theta, \\[2mm] M'_m = \dfrac{1}{\Delta_m\pi}\int_{-\pi}^{\pi}\dfrac{1}{\mu k}\tau_{rz}^{(ff)}\cos m\theta d\theta, \\[2mm] N'_m = \dfrac{1}{\pi}\int_{-\pi}^{\pi}\dfrac{1}{\mu k}\tau_{rz}^{(ff)}\sin m\theta d\theta. \end{cases} \qquad (16)$$

$$\Delta_m = \begin{cases} 2, m = 0 \\ 1, m\neq 0 \end{cases} \qquad (17)$$

Because of the presence of the hill and auxiliary boundary, two extra waves are generated. The first wave is the outgoing waves $W^{(d)}$ in the exterior region S, while the second one is the standing waves $W^{(\Omega)}$ inside the interior region Ω. Both the outgoing waves and standing waves can be expressed as a series form of Bessel functions.

The mathematical form of $W^{(d)}$ is given as follows:

$$W^{(d)} = \sum_{m=0}^{+\infty} H_m^{(1)}(kr)\left(A_m\delta_m^{(1)}\cos m\theta + B_m\delta_m^{(2)}\sin m\theta\right) \qquad (18)$$

where $\delta_m^{(1)} = 1 + (-1)^m$ and $\delta_m^{(2)} = 1 - (-1)^m$ and A_m and B_m are the unknown coefficients.

Relevant stress components are derived as follows:

$$\tau_{\theta z}^{(d)} = \frac{\mu\partial W^{(d)}}{r\partial\theta} = \frac{\mu}{r}\sum_{m=0}^{+\infty} H_m^{(1)}(kr)\left(-A_m\delta_m^{(1)}m\sin m\theta + B_m\delta_m^{(2)}m\cos m\theta\right) \qquad (19)$$

$$\tau_{rz}^{(d)} = \frac{\mu\partial W^{(d)}}{\partial r} = \mu k\sum_{m=0}^{+\infty} H_m'^{(1)}(kr)\left(A_m\delta_m^{(1)}\cos m\theta + B_m\delta_m^{(2)}\sin m\theta\right) \qquad (20)$$

Substituting $\theta = \pm\pi/2$ into Eq. (19) deduces $\tau_{\theta z}^{(d)} = 0$ which indicates the outgoing wave field $W^{(d)}$ satisfies the traction-free boundary condition (Eq. (2)).

The total wave fields $W^{(S)}$ and $\tau_{rz}^{(S)}$ of the exterior region are the superposition of free wave fields and outgoing wave fields, as follows:

$$W^{(S)} = W^{(d)} + W^{(ff)} \qquad (21)$$

$$\tau_{rz}^{(S)} = \tau_{rz}^{(d)} + \tau_{rz}^{(ff)} \qquad (22)$$

The mathematical form of $W^{(\Omega)}$ is given as follows:

$$W^{(\Omega)} = \sum_{m=0}^{+\infty} J_m(kr)(C_m\cos m\theta + D_m\sin m\theta) \qquad (23)$$

where $J_m(\cdot)$ represents the Bessel function with order m, C_m, and D_m are the unknown coefficients.

Relevant stress components are expressed as follows:

$$\tau_{\theta z}^{(\Omega)} = \frac{\mu\partial W^{(\Omega)}}{r\partial\theta} = \frac{\mu}{r}\sum_{m=0}^{+\infty} J_m(kr)(-C_m m\sin m\theta + D_m m\cos m\theta) \qquad (24)$$

$$\tau_{rz}^{(\Omega)} = \frac{\mu\partial W^{(\Omega)}}{\partial r}$$
$$= \mu k\sum_{m=0}^{+\infty} J_m'(kr)(C_m\cos m\theta + D_m\sin m\theta) \qquad (25)$$

Now, defining two functions $\Phi(\theta)$ and $\Psi(\theta)$ as follows:

$$\Phi(\theta) = \begin{cases} 0, -\pi/2 + 2l\pi\leq\theta\leq\pi/2 + 2l\pi \\ W^{(\Omega)}(a,\theta) - W^{(S)}(a,\theta), \text{ other} \end{cases}, l = 0, \pm 1, \pm 2, \ldots \qquad (26)$$

$$\Psi(\theta) = \begin{cases} \tau_{rz}^{(\Omega)}(a,\theta), -\pi/2 + 2l\pi\leq\theta\leq\pi/2 + 2l\pi \\ \tau_{rz}^{(\Omega)}(a,\theta) - \tau_{rz}^{(S)}(a,\theta), \text{ other} \end{cases}, l = 0, \pm 1, \pm 2, \ldots \qquad (27)$$

According to Eqs. (3) and (4), the values of $\Phi(\theta)$ and $\Psi(\theta)$ are equal to zero. Expanding $\Phi(\theta)$ and $\Psi(\theta)$ into Fourier series over interval $[-\pi,\pi]$ and making the coefficients of the series equal to zero can lead to the following equations:

$$\sum_{m=0}^{+\infty}\left[H_m^{(1)}(ka)A_m\delta_m^{(1)} - C_m J_m(ka) + M_m\right]\lambda_{mn} = 0 \qquad (28)$$

$$\sum_{m=0}^{+\infty}\left[H_m^{(1)}(ka)B_m\delta_m^{(2)} - D_m J_m(ka) + N_m\right]\mu_{mn} = 0 \qquad (29)$$

$$C_n J_n'(ka) - \sum_{m=0}^{+\infty}\left[H_m'^{(1)}(ka)A_m\delta_m^{(1)} + M'_m\right]\lambda_{mn} = 0 \qquad (30)$$

$$D_n J_n'(ka) - \sum_{m=0}^{+\infty}\left[H_m'^{(1)}(ka)B_m\delta_m^{(2)} + N'_m\right]\mu_{mn} = 0 \qquad (31)$$

where

$$\lambda_{mn} = \begin{cases} \dfrac{1}{2}, & m = n \\[3mm] \dfrac{\varepsilon_n}{2\pi}\dfrac{-2m\cos\dfrac{n\pi}{2}\sin\dfrac{m\pi}{2} + 2n\cos\dfrac{m\pi}{2}\sin\dfrac{n\pi}{2}}{m^2 - n^2}, & m\neq n \end{cases} \qquad (32)$$

$$\mu_{mn} = \begin{cases} 0, & m = n = 0 \\ \dfrac{1}{2}, & m = n \neq 0 \\ \dfrac{\varepsilon_n}{2\pi} \dfrac{-2n\cos\frac{n\pi}{2}\sin\frac{m\pi}{2} + 2m\cos\frac{m\pi}{2}\sin\frac{n\pi}{2}}{m^2-n^2}, & m \neq n \end{cases} \tag{33}$$

$$\varepsilon_n = \begin{cases} 1, & n = 0 \\ 2, & n \neq 0 \end{cases} \tag{34}$$

Then, substituting Eqs. (30) and (31) into Eqs. (28) and (29) derives the following equations:

$$\sum_{m=0}^{+\infty} \delta_m^{(1)} \left[H_m^{(1)}(ka)\lambda_{mn} - H_m'^{(1)}(ka)P_{mn} \right] A_m$$
$$= \sum_{m=0}^{+\infty} -M_m\lambda_{mn} + M_m' P_{mn} \tag{35}$$

$$\sum_{m=0}^{+\infty} \delta_m^{(2)} \left[H_m^{(1)}(ka)\mu_{mn} - H_m'^{(1)}(ka)Q_{mn} \right] B_m$$
$$= \sum_{m=0}^{+\infty} -N_m\mu_{mn} + N_m' Q_{mn} \tag{36}$$

where

$$P_{mn} = \sum_{l=0}^{+\infty} \frac{J_l(ka)}{J_l'(ka)} \lambda_{ml}\lambda_{ln} \tag{37}$$

$$Q_{mn} = \sum_{l=0}^{+\infty} \frac{J_l(ka)}{J_l'(ka)} \mu_{ml}\mu_{ln} \tag{38}$$

and $m, n = 0, 1, 2, \dots$

The unknown coefficients A_m and B_m can be solved numerically by truncating Eqs. (35) and (36) into finite terms. Specifically, the indexes m and n are truncated to M and N terms, where M is the number of truncation of series solutions and N is the number of equations. Besides, N should be greater than M; thus the truncated equations become over-determined and should be solved by the least-squares method.

After solving Eqs. (35)–(36) and obtaining the value of coefficients A_m and B_m, the unknown coefficients C_n and D_n can be deduced from Eqs. (30) and (31) as follows:

$$C_n = \frac{1}{J_n'(ka)} \sum_{m=0}^{+\infty} \left[H_m'^{(1)}(ka)A_m\delta_m^{(1)} + M_m' \right]\lambda_{mn} = 0 \tag{39}$$

$$D_n = \frac{1}{J_n'(ka)} \sum_{m=0}^{+\infty} \left[H_m'^{(1)}(ka)B_m\delta_m^{(2)} + N_m' \right]\mu_{mn}$$
$$= 0 \tag{40}$$

Finally, we can calculate the wave field at any point within the theoretical model by Eqs. (21) and (23).

Validation of theoretical solution

The accuracy of the series solution can be verified by checking the correctness of the displacement and stress continuous conditions at the auxiliary boundary. Because the value of the incident waves $W^{(i)}$ is frequency-dependent, and obviously not equal to 1, we take the normalized displacement residuals ΔW and stress residuals $\Delta\tau_{rz}$ at the auxiliary boundary as follows:

$$\Delta W = \left| W^{(\Omega)} - W^{(S)} \right| / W_0 \tag{41}$$

$$\Delta\tau_{rz} = \left| \tau_{rz}^{(\Omega)} - \tau_{rz}^{(S)} \right| / \tau_0 \tag{42}$$

where $W_0 = 2\left| W^{(i)}(0,0) \right| = \left| i/2\mu H_0^{(1)}(kr_0) \right|$ is the value of the free field displacement $W^{(ff)}$ at the origin of the Cartesian coordinate system (x, y) and $\tau_0 = \mu k W_0$.

To reduce the number of variables, the dimensionless frequency is defined as follows:

$$\eta = \frac{2a}{\lambda} = \frac{ka}{\pi} \tag{43}$$

where $\lambda = 2\pi/k$ is the wavelength of the incident waves.

Figures 2, 3, 4 illustrate the variations of the displacement residuals ΔW and stress residuals $\Delta\tau_{rz}$ at the auxiliary boundary with increasing truncation order M when line source is located at $r_0 = 2a$, $\theta_0 = -180^{\circ}$ and the values of dimensionless frequencies are $\eta = 1.0$, 2.0 and 3.0, respectively. The abscissa in the figures is the angle variable θ ranging from 90° to 270°.

As seen in Figs. 2, 3, 4, as the truncation order M increases, the displacement residuals ΔW and the stress residuals $\Delta\tau_{rz}$ gradually decrease to a small number, which means the error of series solution is negligible provided M is large enough. Note that the values of ΔW and $\Delta\tau_{rz}$ at the rims of the hill ($\theta = 90^{\circ}$ or 270°) are significantly higher than the rest of the auxiliary boundary. This is because the included angles of the rims are greater than π and it can cause stress singularity. Fortunately, the influence of stress singularity on the accuracy of the displacement solutions is comparatively small because the displacements at the rims are finite. Therefore, the displacement solution can relatively quickly converge to the true solution (Yuan and Liao 1996).

Results and discussion

In this section, the displacement distribution on surface and interior of the hill are systematically discussed for different dimensionless frequencies and source locations. Consistent with the above section, the displacement amplitude $|W|$ is normalized by W_0.

Fig. 2 The normalized displacement residuals and stress residuals at the auxiliary boundary when $\eta = 1.0$

(a)

(b)
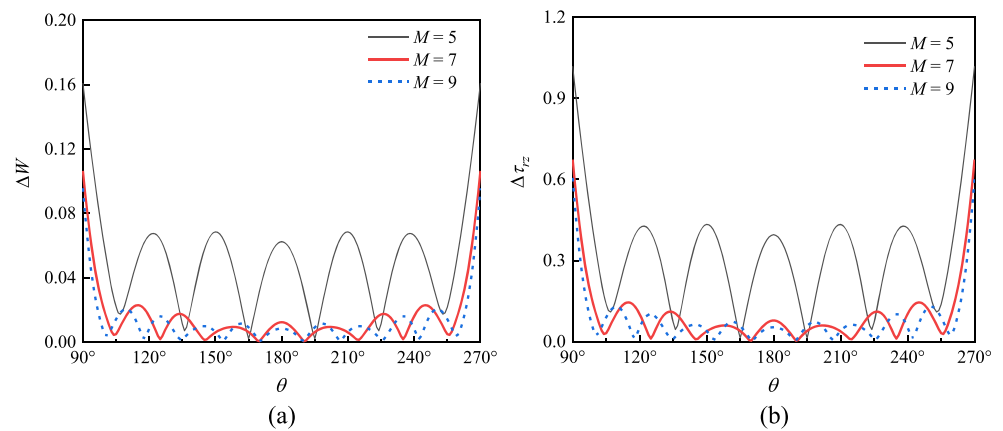
## The comparison of surface displacement induced by cylindrical waves and plane waves

Figure 5 demonstrates the normalized amplitudes of surface displacement of half-space ($-3 \leq y/a \leq -3$) induced by the plane waves (Yuan and Men 1992) and cylindrical waves. The solid lines represent the case of the plane waves and short dashed and dashed lines correspond to the case of the cylindrical waves with source distance $r_0 = 2a$, $15a$.

As seen in Fig. 5, the surface displacement distribution for near-source ($r_0 = 2a$) cylindrical waves is quite different from that of plane waves. The displacement amplitudes on hill surface excited by the near-source cylindrical waves are generally smaller than those excited by the plane waves when the incident direction is vertical to half-space. However, when the incident direction is oblique or horizontal to half-space, the displacement amplitudes on hill surface caused by the near-source cylindrical waves are larger than those caused by the plane waves. For example, the displacement amplitudes at the hilltop ($y/a = 0$) are 1.96 for plane waves (solid line) and 1.74 for near-source cylindrical waves (short dashed line) in Fig. 5(d). But those values in Figs. 5(e) and (f) are 0.66 versus 0.86 and 0.40 versus 0.58, respectively. Moreover, when the dimensionless frequency is high, the topographic effect at

certain locations for the plane waves and near-source cylindrical wave is contrary. For instance, as shown in Fig. 5(g), when the dimensionless frequency $\eta = 2.0$, the displacement amplitudes at the hilltop are 1.32 for plane waves and 0.53 for near-source cylindrical waves. In addition, those values are 0.13 versus 1.38 in Fig. 5(j). The above results indicate that we cannot simply view the cylindrical waves as plane waves, and the influence of source distance on amplitudes should be handled.

Then, we compare the results for far-source ($r_0 = 15a$) cylindrical waves (dashed line) and plane waves (solid lines). The surface displacements between them are in good accord, except a little difference on the horizontal ground due to the geometric attenuation effect of the cylindrical waves. The average differences in the surface displacements ($-3 \leq y/a \leq -3$) between far-source cylindrical waves and plane waves are only 1.94, 3.48, and 4.01% in Figs. 5(a)–(c), and those values in (d)–(f) are 2.32, 7.10, and 4.39%, in Figs. 5(g)-(i) are 5.87, 4.87, and 6.33% and in Figs. 5(j)–(l) are 5.67, 4.70, and 4.38%. Since these values are small, e.g., most of them are less than 5% and the maximum is only 7.10%, one can conclude that the cylindrical waves can be regarded as the plane waves when the source distance is greater than 15 times the hill radius.

Fig. 3 The normalized displacement residuals and stress residuals at the auxiliary boundary when $\eta = 2.0$

(a)

(b)
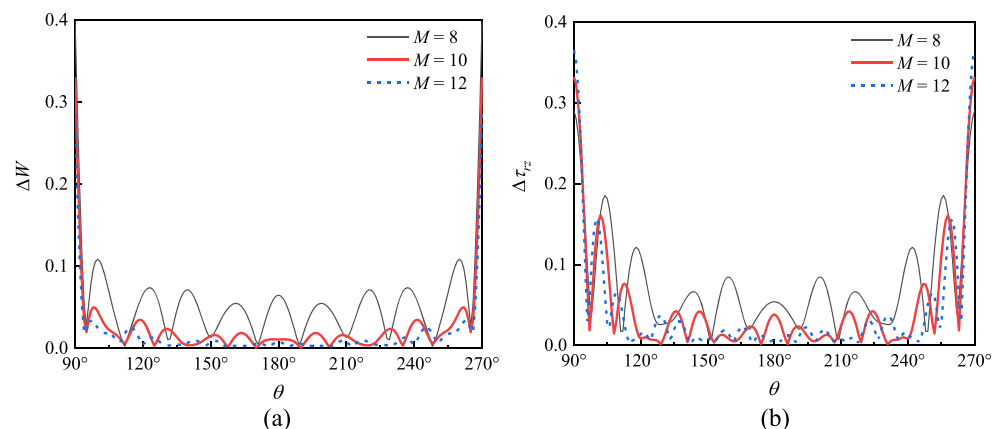
Fig. 4 The normalized displacement residuals and stress residuals at the auxiliary boundary when $\eta = 3.0$

(a)

(b)
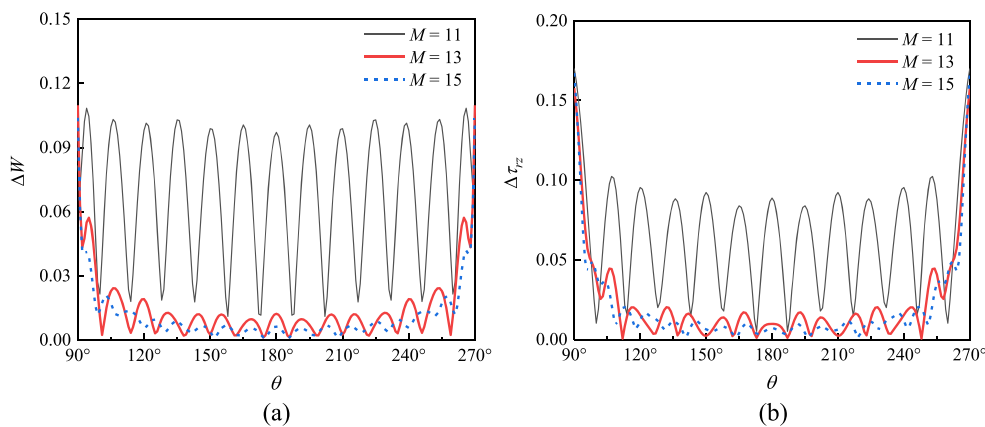
The relationship between the surface displacement and dimensionless frequency

The main influencing factors on the responses of the semi-circular hill are incident wave frequency, radius of the hill and source location. In previous subsection, the effects of source location on displacement amplitudes have been investigated. This subsection focuses on the effects of incident wave frequency and radius of the hill, and they are expressed by the dimensionless frequency.

Fig. 6 shows the normalized amplitudes of surface displacement of half-space ($-3 \leq y/a \leq -3$) for different dimensionless frequencies when source distance $r_0 = 5a$ and source angles $\theta_0 = -180^o$, -135°, -90°, respectively.

As depicted in Fig. 6, when the dimensionless frequency is not greater than 1.0, the displacement amplitudes variation along surface is relatively slow and only one single peak value is observed on hill surface. For example, when the dimensionless frequency $\eta = 0.2$, the surface displacement peaks for $\theta_0 = -180^o$, -135°, and -90° are 1.49, 1.45, and 1.40, and all of them appear near at the hilltop ($y/a = 0$), and the average differences in displacement amplitudes between hilltop and other points of hill surface are only 6.17, 6.45, and 6.73%, respectively. Besides, the source angles have significant impact on the location and corresponding frequency of the maximum displacements. For instance, the maximum displacement in Figs. 6(a) and (b) is 1.891 located at $y/a = 0$ and $\eta = 1.0$, in Figs. 6(c) and (d) is 1.796 located at $y/a = 0.77$ and $\eta = 0.7$, and in Figs. 6(e) and (f) is 1.803 located at $y/a = 0.88$ and $\eta = 0.7$. The above results indicate that the topographic amplification effects widely exist for different source angles when the dimensionless frequency is not greater than 1.0.

Then, we can see that when the dimensionless frequency is greater than 1.0, there are multiple displacement peaks on hill surface, and the number of the peaks increase as the dimensionless frequency increases. Furthermore, the displacement peaks for $\theta_0 = -180^o$ are large, and significant topographic amplification effects are observed, while the displacement peaks for $\theta_0 = -90^o$ are small and mostly show the topographic

reduction effects. It makes sense because the wave energy is primarily concentrated in the incident direction, and the energy of the diffraction wave will decrease as the incident wave frequency increases. Therefore, the displacement amplitudes for $\theta_0 = -180^o$ is generally greater than that for $\theta_0 = -90^o$, especially when the dimensionless frequency is large.

The relationship between the internal displacement and dimensionless frequency

Due to the difference of wave propagation path, the displacement distributions of the interior and surface of the hill are different. Figure 7 illustrates the normalized amplitudes of internal displacement along vertical direction ($\theta = 0^o$) of the semi-circular hill for different dimensionless frequencies when $r_0 = 5a$ and $\theta_0 = -180^o$, -135°, and -90°, respectively.

As shown in Fig. 7, when the dimensionless frequency $\eta \leq 0.5$, the displacement will increase monotonously with increasing elevation, and the maximum displacement appears at the hill surface ($x/a = 1.0$). But this monotonicity will be altered with the increased dimensionless frequency, and the internal displacement is possibly greater than the surface displacement. For example, when $\eta \geq 0.5$, as the elevation increases, the displacement for $\theta_0 = -90^o$ first decreases then increases, and the maximum displacement appears at the hill bottom ($x/a = 0.0$) rather than the hill surface. Moreover, the characteristics of displacement distribution vary with source angles. For instance, when $\eta \geq 2.0$, the displacements for $\theta_0 = -180^o$ are large in the middle and small at both ends, and the maximum displacements appear near $x/a = 0.5$, showing significant amplitude amplification effects, while the surface displacements exhibit amplitude reduction effects. On the contrary, the displacements for $\theta_0 = -135^o$ and -90° are small in the middle and large at both ends, and the maximum displacements appear at the hill surface or hill bottom. Above results indicate that the surface displacements are possibly smaller than the internal displacements when the dimensionless frequency is large. Especially when the source is located directly
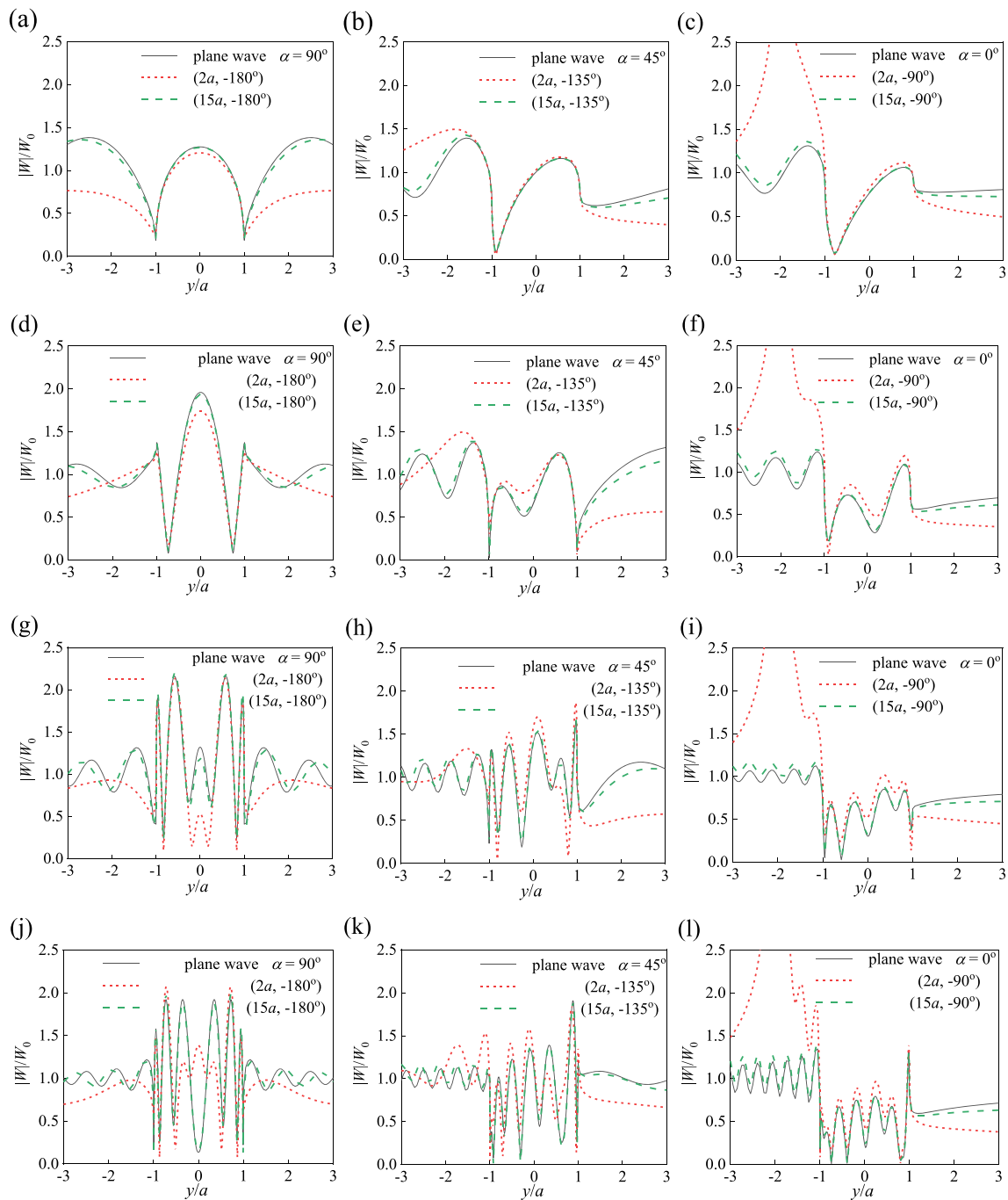
Fig. 5 Comparison of normalized amplitudes of surface displacement for a semi-circular hill subject to plane *SH* waves and cylindrical *SH* waves. The incident angles α of the plane waves and the source locations (r_0, θ_0) of the cylindrical waves are given. The results in (**a**)–(**c**) are for dimensionless frequency $\eta = 0.5$, and those in (**d**)–(**f**), (**g**)–(**i**), (**j**)–(**l**) correspond to $\eta = 1.0, 2.0,$ and 3.0, respectively

below the hill, the surface displacements are reduced but the internal displacements could be amplified.

## The displacements induced by transient waves

In above subsections, we have analyzed the effects of steady waves on the distribution of surface and internal displacements of semi-circular hill. However, the actual seismic waves are transient waves, and the results of single frequency are unable to fully embody the features of transient motions. In this subsection, the transient responses for semi-circular hill are given through the inverse fast Fourier Transform.

The incident wave is assumed as Ricker wavelet:

$$R(t) = \left(2\pi^2 f_c^2 t^2 - 1\right)\exp\left(-\pi^2 f_c^2 t^2\right) \tag{44}$$
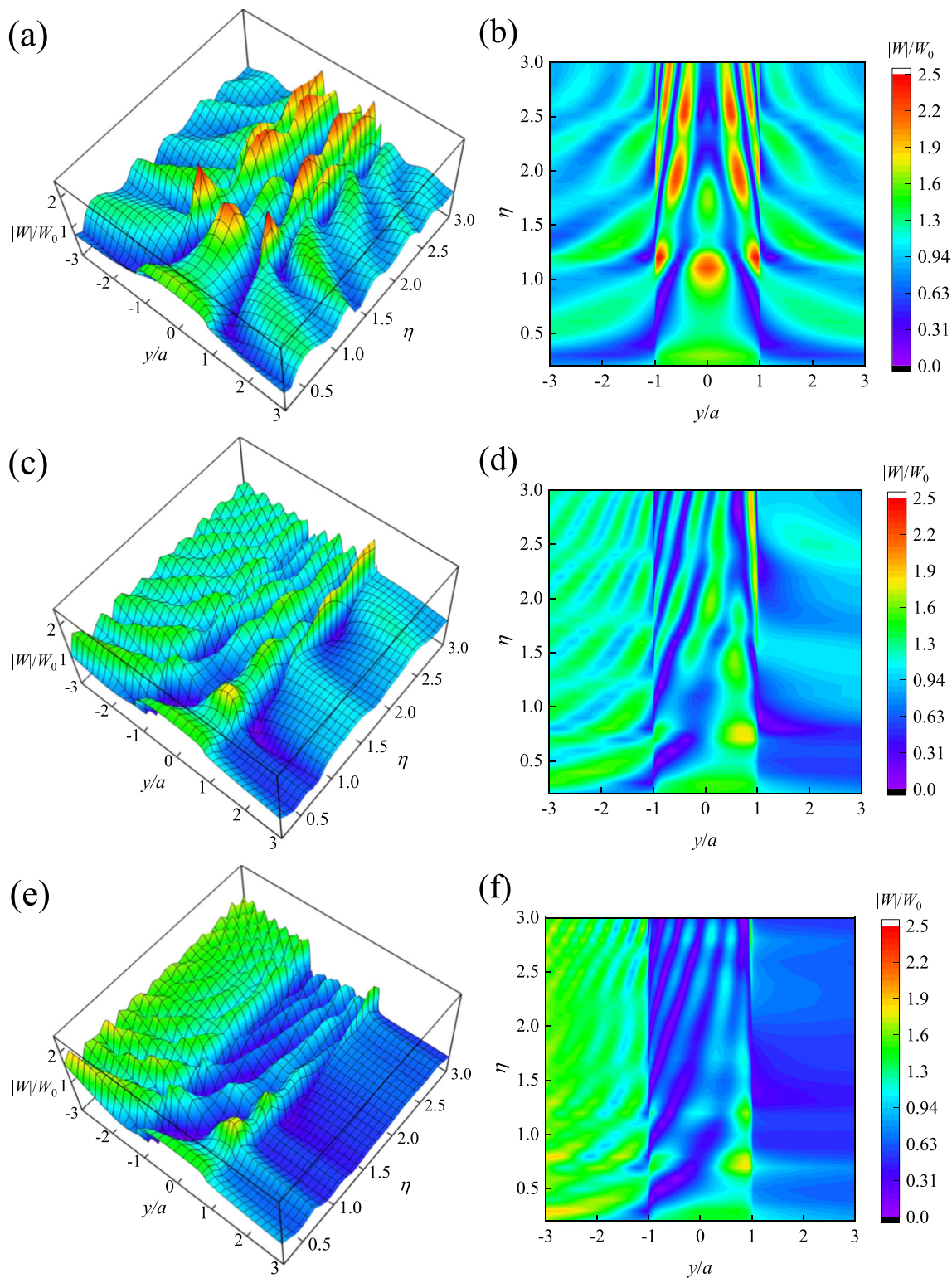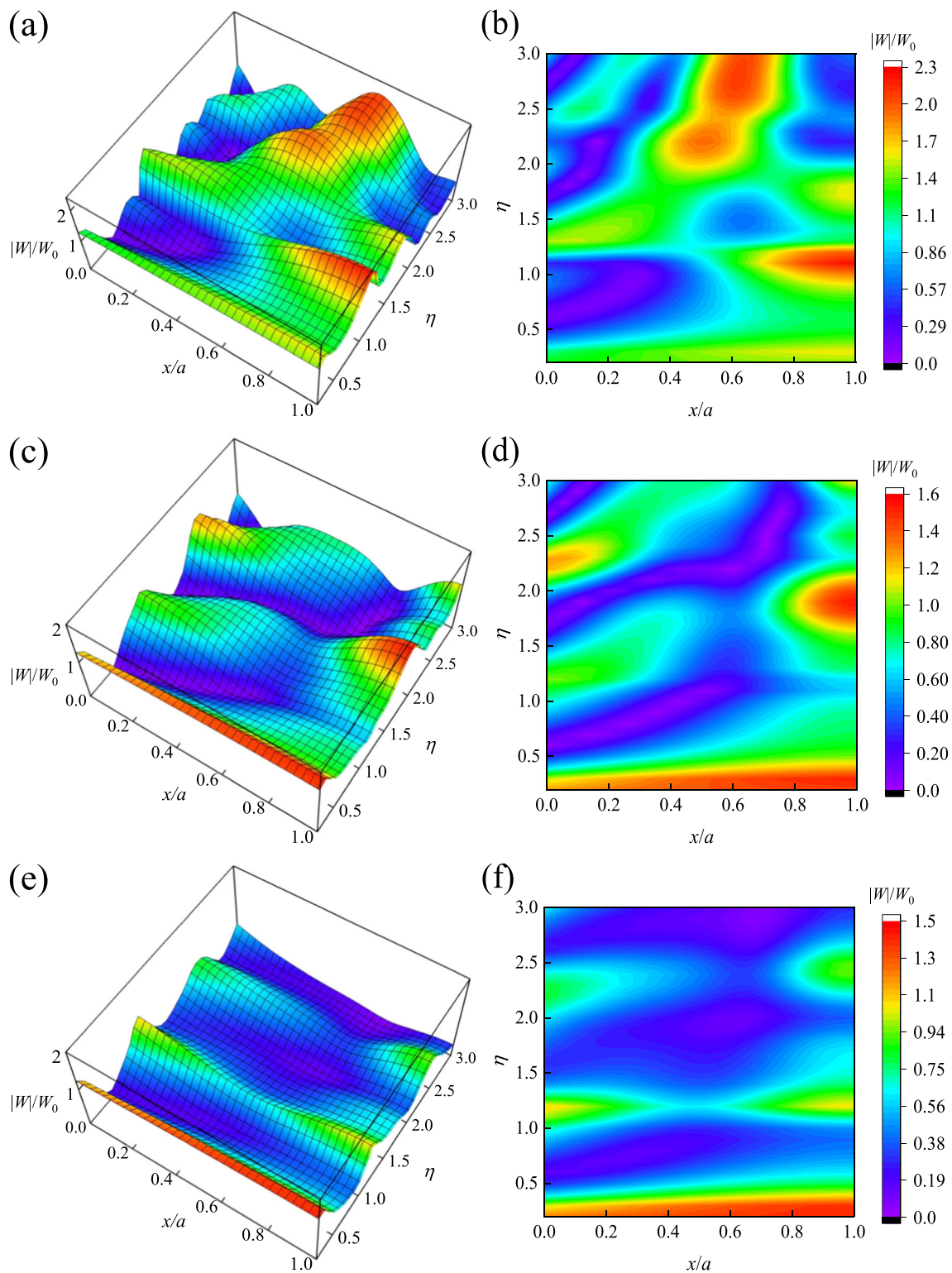
Fig. 6 The normalized amplitudes of surface displacement for a semi-circular hill with different dimensionless frequencies. The results in (**a**)–(**b**) are for source location ($r_0 = 5a$, $\theta_0 = -180°$) and those in (**c**)–(**d**) and (**e**)–(**f**) correspond to ($r_0 = 5a$, $\theta_0 = -135°$) and ($r_0 = 5a$, $\theta_0 = -90°$), respectively

where $f_c = 1.0$Hz represents the predominant frequency.

Because the amplitude spectrum of the wavelet is approximate to zero at 4Hz, we take the calculation frequencies ranging from 0 4Hz and the interval is 1/24Hz. For comparison, both the dimensionless frequencies for transient waves $\eta_c = 2af_c/c$ and steady waves $\eta = 2af/c$ are set to 1.0. Figure 8
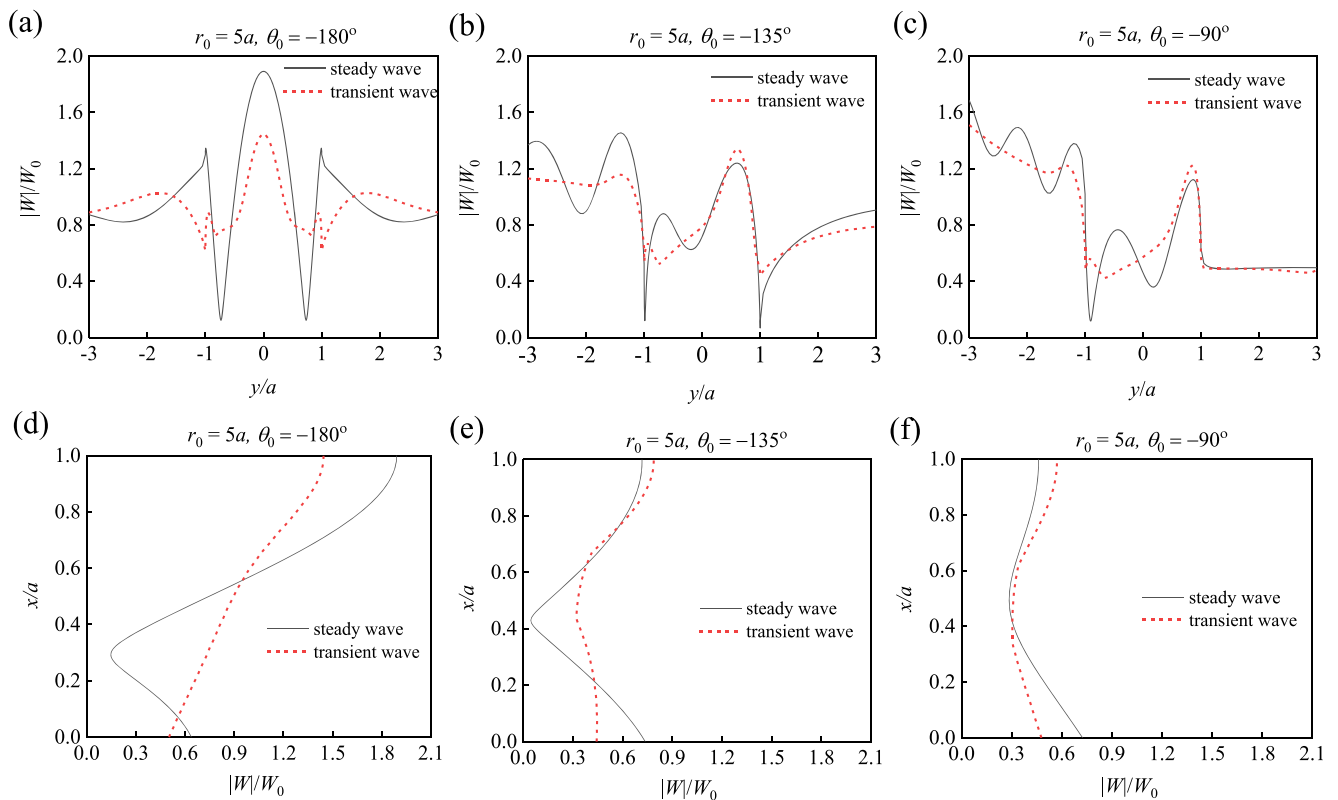
Fig. 7 The normalized amplitudes of internal displacement along vertical direction ($\theta = 0^\circ$) of the semi-circular hill with different dimensionless frequencies. The results in (**a**)-(**b**) are for source location ($r_0 = 5a$, $\theta_0 = -180^\circ$), and those in (**c**)-(**d**) and (**e**)-(**f**) correspond to ($r_0 = 5a$, $\theta_0 = -135^\circ$) and ($r_0 = 5a$, $\theta_0 = -90^\circ$), respectively

shows normalized amplitudes of displacement around the hill caused by transient waves and steady waves when $r_0 = 5a$ and $\theta_0 = -180^\circ$, -135°, and -90°, respectively.

As illustrated in Fig. 8, the overall distribution of displacement amplitudes of transient responses and steady responses is consistent, but there are some differences.

Fig. 8 Comparison of transient waves and steady waves on displacement distributions of the semi-circular hill when the dimensionless frequency $\eta = 1.0$. The results in (**a**)-(**c**) are surface displacements, and those in (**d**)-(**f**) correspond to internal displacements along vertical direction ($\theta = 0^\circ$)

Firstly, the amplitude fluctuations of the transient waves are lower than those of steady waves. For example, in Fig. 8(a), the maximum differences in displacement amplitudes on hill surface are equal to 1.77 and 0.82 for steady waves and transient waves, respectively. Secondly, the maximum responses of transient waves are less than that of steady waves for $\theta_0 = -180^\circ$, but it is contrary for $\theta_0 = -135^\circ$ and -90°. For example, the maximum displacements for transient waves and steady waves in Fig. 8(a) are 1.44 and 1.89, in Fig. 8(b) are 1.34 and 1.24, and in Fig. 8(c) are 1.23 and 1.11. That is because for steady waves with $\eta = 1.0$, the maximum displacement for $\theta_0 = -180^\circ$ is at a peak along η-axis (as seen in Fig. 6(a)). Therefore, transient waves which contain other frequencies have a lower amplitude than steady waves. While the maximum displacement for $\theta_0 = -135^\circ$ and -90° are located in the middle of two peaks along η-axis (as seen in Figs. 6(c) and (e)), thus transient waves have a larger amplitude than steady waves. Thirdly, the displacement amplitudes at the hill bottom ($x/a = 0.0$) for transient waves are less than those for steady waves. It could be due to the transient waves are finite wave trains, while the steady waves are infinite wave trains, therefore the intensity of wave superposition at the hill bottom of the transient waves is lower than that of steady waves.

Conclusions

In this paper, a novel series solution for the dynamic response of semi-circular hill subject to the cylindrical *SH* wave is derived by wave expansion method. The influence of source location and dimensionless frequency on displacement distributions around the hill is systematically analyzed. The main conclusions are drawn as follows:

(1) When the source distance is small, the displacements of the hill surface caused by cylindrical waves are generally smaller than those caused by plane waves for the case of vertical incidence, but it is contrary to the cases of oblique incidence and horizontal incidence. As source distance increases, the difference between them decreases. When the source distance is larger than 15 times of the radius of the hill, this difference is negligible.

(2) When the dimensionless frequency is not greater than 1.0, the topographic amplification effects widely exist in different source angles. But when the dimensionless frequency is greater than 1.0, the topographic amplification effects mainly occur in the case of vertical incidence, and the case of horizontal incidence mainly exhibits topographic reduction effects.

(3) The displacements of hill surface are larger than the displacements inside the hill when the dimensionless

frequency is not larger than 1.0, and when the dimensionless frequency is larger than 1.0, the displacements of hill surface are possibly smaller than that inside the hill.

(4) When the predominant frequency of transient waves is the same with the frequency of steady waves, the displacement amplitude distributions of the hill caused by transient and steady waves are consistent on the whole, but there are some differences, such as the amplitude fluctuations of the former is lower than that of the latter.

Authors' contributions
• Conceptualization: [Zhiwen Li]
• Methodology: [Zhiwen Li]
• Formal analysis and investigation: [Zhiwen Li], [Haibo Li]
• Writing - original draft preparation: [Zhiwen Li]
• Writing - review and editing: [Zhiwen Li]
• Funding acquisition: [Haibo Li]
• Resources: [Haibo Li]
• Supervision: [Haibo Li]

Data Availability Not applicable

Code availability Not applicable

Declarations

Conflicts of interest The authors declare that they have no known competing financial interests or personal relationships that could have appeared to influence the work reported in this paper.

References

Amornwongpaibun A, Lee VW (2013) Scattering of anti-plane (SH) waves by a semi-elliptical hill: II—deep hill. Soil Dyn Earthq Eng 52:126–137. https://doi.org/10.1016/j.soildyn.2012.08.006

Boore DM (1972) A note on the effect of simple topography on seismic SH waves. Bull Seismol Soc Am 62(1):275–284. https://doi.org/10.4028/www.scientific.net/amr.378-379.789

Cao H, Lee VW (1989) Scattering of plane SH waves by circular cylindrical canyons with variable depth-to-width ratio. Eur Earthq Eng 3(2):29–37

Cao H, Lee VW (1990) Scattering and diffraction of plane P waves by circular cylindrical canyons with variable depth-to-width ratio. Soil Dyn Earthq Eng 9(3):141–150. https://doi.org/10.1016/s0267-7261(09)90013-6

Cavallaro A, Ferraro A, Grasso S et al (2008) Site response analysis of the Monte Po Hill in the City of Catania. In AIP Conference Proceedings. Am Inst Physics 1020(1):240–251. https://doi.org/10.1063/1.2963841

Ferraro A, Grasso S, Maugeri M (2009) Seismic Vulnerability of a slope in Central Italy. In Proc. First International Conference on Disaster Management and Human Health. New Forest, UK 345-356. https://doi.org/10.2495/dman090301

Gao YF, Zhang N (2013) Scattering of cylindrical SH waves induced by a symmetrical V-shaped canyon: near-source topographic effects. Geophys J Int 193(2):874–885. https://doi.org/10.1093/gji/ggs119

Gao YF, Zhang N, Li DY, Cai YQ, Wu YX (2012) Effects of topographic amplification induced by a U-shaped canyon on seismic waves. Bull Seismol Soc Am 102(4):1748–1763. https://doi.org/10.1785/0120110306

Geli L, Bard PY, Jullien B (1988) The effect of topography on earthquake ground motion: a review and new results. Bull Seismol Soc Am 78(1):42–63. https://doi.org/10.1016/0148-9062(88)90024-1

Hayir A, Todorovska MI, Trifunac MD (2001) Antiplane response of a dike with flexible soil-structure interface to incident SH waves. Soil Dyn Earthq Eng 21(7):603–613. https://doi.org/10.1016/s0267-7261(01)00035-5

Hough SE, Altidor JR, Anglade D et al (2010) Localized damage caused by topographic amplification during the 2010 M 7.0 Haiti earthquake. Nature Geoscience 3(11): 778. 10.1038/ngeo988

Komatitsch D, Vilotte JP (1998) The spectral element method: an efficient tool to simulate the seismic response of 2D and 3D geological structures. Bull Seismol Soc Am 88(2):368–392. https://doi.org/10.1190/1.1820185

Le T, Lee VW, Trifunac MD (2017) SH waves in a moon-shaped valley. Soil Dyn Earthq Eng 101:162–175. https://doi.org/10.1016/j.soildyn.2017.06.019

Lee VW, Amornwongpaibun A (2013) Scattering of anti-plane (SH) waves by a semi-elliptical hill: I—Shallow hill. Soil Dyn Earthq Eng 52:116–125. https://doi.org/10.1016/j.soildyn.2012.08.005

Lee VW, Cao H (1989) Diffraction of SV waves by circular canyons of various depths. J Eng Mech 115(9):2035–2056

Lee VW, Luo H, Liang J (2006) Antiplane (SH) waves diffraction by a semicircular cylindrical hill revisited: an improved analytic wave series solution. J Eng Mech 132(10):1106–1114. https://doi.org/10.1061/(asce)0733-9399(2006)132:10(1106)

Li H, Liu Y, Liu L et al (2019a) Numerical evaluation of topographic effects on seismic response of single-faced rock slopes. Bull Eng Geol Environ 78(3):1873–1891. https://doi.org/10.1007/s10064-017-1200-7

Li L, Ju N, Zhang S et al (2019b) Shaking table test to assess seismic response differences between steep bedding and toppling rock slopes. Bull Eng Geol Environ 78(1):519–531. https://doi.org/10.1007/s10064-017-1186-1

Liang J, Li FJ, Gu XL (2005a) Scattering of Rayleigh waves by a shallow circular canyon: High-frequency solution. Earthq Eng Eng Vib 25(5):24. https://doi.org/10.1007/s11589-002-0183-y

Liang J, Zhang Y, Lee VW (2005b) Scattering of plane P waves by a semi-cylindrical hill: analytical solution. Earthq Eng Eng Vib 4:27–36. https://doi.org/10.1007/s11803-005-0021-z

Liang J, Zhang Y, Lee VW (2006) Surface motion of a semi-cylindrical hill for incident plane SV waves: Analytical solution. Acta Seismol Sin 19(3):251–263. https://doi.org/10.1007/s11589-003-0251-y

Lin S, Qiu FQ, Liu DK (2010) Scattering of SH waves by a scalene triangular hill. Earthq Eng Eng Vib 9(1):23–38. https://doi.org/10.1007/s11803-009-8091-y

Massa M, Barani S, Lovati S (2014) Overview of topographic effects based on experimental observations: meaning, causes and possible interpretations. Geophys J Int 197(3):1537–1550. https://doi.org/10.1093/gji/ggt341

Mow CC, Pao YH (1971) The diffraction of elastic waves and dynamic stress concentrations. Report R-482-PR. The Rand Corporation, Santa Monica, California.

Opršal I, Zahradník J (1999) Elastic finite-difference method for irregular grids. Geophysics 64(1):240–250. https://doi.org/10.1190/1.1444520

Panji M, Kamalian M, Asgari MJ, Jafari MK (2014) Analysing seismic convex topographies by a half-plane time-domain BEM. Geophys J Int 197(1):591–607. https://doi.org/10.1093/gji/ggu012

Qiu FQ, Liu DK (2005) Antiplane response of isosceles triangular hill to incident SH waves. Earthq Eng Eng Vib 4(1):37–46. https://doi.org/10.1109/spawda.2019.8681846

Todorovska MI, Lee VW (1991) A note on scattering of Rayleigh waves by shallow circular canyons: analytical approach. Bull Indian Soc Earthquake Technol 28(2):1–16

Trifunac MD (1972) Scattering of plane SH waves by a semi-cylindrical canyon. Earthq Eng Struct Dyn 1(3):267–281

Trifunac MD, Hudson DE (1971) Analysis of the Pacoima dam accelerogram—San Fernando, California, earthquake of 1971. Bull Seismol Soc Am 61(5):1393–1411

Tsaur DH, Chang KH (2008) An analytical approach for the scattering of SH waves by a symmetrical V-shaped canyon: shallow case. Geophys J Int 174(1):255–264. https://doi.org/10.1111/j.1365-246x.2008.03788.x

Tsaur DH, Chang KH (2010) An analytical approach for the scattering of SH waves by a symmetrical V-shaped canyon: deep case. Geophys J Int 183(3):1501–1511. https://doi.org/10.1111/j.1365-246x.2010.04806.x

Wong HL, Jennings PC (1975) Effects of canyon topography on strong ground motion. Bull Seismol Soc Am 65(5):1239–1257

Wong HL, Trifunac MD (1974) Scattering of plane SH waves by a semi-elliptical canyon. Earthq Eng Struct Dyn 3(2):157–169. https://doi.org/10.1002/eqe.4290030205

Yuan XM, Liao ZP (1994) Scattering of plane SH waves by a cylindrical canyon of circular-arc cross-section. Soil Dyn Earthq Eng 13(6):407–412. https://doi.org/10.1016/0267-7261(94)90011-6

Yuan XM, Liao ZP (1996) Surface motion of a cylindrical hill of circular—arc cross-section for incident plane SH waves. Soil Dyn Earthq Eng 15(3):189–199. https://doi.org/10.1016/0267-7261(95)00040-2

Yuan XM, Men FL (1992) Scattering of plane SH waves by a semi-cylindrical hill. Earthq Eng Struct Dyn 21(12):1091–1098. https://doi.org/10.1002/eqe.4290211205

Zhang N, Gao YF, Cai YQ, Li DY, Wu YX (2012a) Scattering of SH waves induced by a non-symmetrical V-shaped canyon. Geophys J Int 191(1):243–256. https://doi.org/10.1111/j.1365-246x.2012.05604.x

Zhang N, Gao YF, Li DY, Wu YX, Zhang F (2012b) Scattering of SH waves induced by a symmetrical V-shaped canyon: a unified analytical solution. Earthq Eng Eng Vib 11(4):445–460. https://doi.org/10.1007/s11803-012-0135-z

Zhang N, Gao YF, Yang J, Yang J, Xu CJ (2015) An analytical solution to the scattering of cylindrical SH waves by a partially filled semi-circular alluvial valley: near-source site effects. Earthq Eng Eng Vib 14(2):189–201. https://doi.org/10.1007/s11803-015-0016-3